


# Monocrystalline Freestanding Three-Dimensional Yttrium-Iron-Garnet Magnon Nanoresonators

F. Heyroth,<sup>1</sup> C. Hauser,<sup>2</sup> P. Trempler,<sup>2</sup> P. Geyer,<sup>2</sup> F. Syrowatka,<sup>1</sup> R. Dreyer,<sup>2</sup> S.G. Ebbinghaus,<sup>3</sup> G. Woltersdorf,<sup>2</sup> and G. Schmidt<sup>1,2,\*</sup>

<sup>1</sup>*Interdisziplinäres Zentrum für Materialwissenschaften, Martin-Luther-Universität Halle-Wittenberg, D-06120 Halle, Germany*

<sup>2</sup>*Institut für Physik, Martin-Luther-Universität Halle-Wittenberg, D-06120 Halle, Germany*

<sup>3</sup>*Institut für Chemie, Martin Luther Universität Halle-Wittenberg, D-06120 Halle, Germany*

 (Received 21 February 2018; revised manuscript received 17 July 2019; published 13 November 2019)

Nanoresonators in which mechanical vibrations and spin waves can be coupled are an intriguing concept that can be used in quantum information processing to transfer information between different states of excitation. Until now, the fabrication of freestanding magnetic nanostructures that host long-lived spin-wave excitations and may be suitable as mechanical resonators has seemed elusive. We demonstrate the fabrication of freestanding monocrystalline yttrium-iron-garnet (YIG) three-dimensional (3D) nanoresonators with nearly ideal magnetic properties. The freestanding 3D structures are obtained using a complex lithography process including room-temperature deposition and lift-off of amorphous YIG and subsequent crystallization by annealing. The crystallization nucleates from the substrate and propagates across the structure even around bends over distances of several micrometers to form, e.g., monocrystalline resonators, as shown by transmission electron microscopy. Spin-wave excitations in individual nanostructures are imaged by time-resolved scanning Kerr microscopy. The narrow line width of the magnetic excitations indicates a Gilbert damping constant of only  $\alpha = 2.6 \times 10^{-4}$ , rivaling the best values obtained for epitaxial YIG thin-film material. The fabrication process represents a step forward in magnonics and magnon mechanics as it provides 3D YIG structures of a high quality. At the same time, it demonstrates an alternative route toward the fabrication of freestanding crystalline nanostructures, which may be applicable also to other material systems.

DOI: [10.1103/PhysRevApplied.12.054031](https://doi.org/10.1103/PhysRevApplied.12.054031)

## I. INTRODUCTION

Nanomechanical oscillators are useful tools for quantum information processing. Over the past decade, numerous groups have, for example, demonstrated the conversion of quantum information from the microwave to the optical regime by means of a micromechanical resonator [1–4]. By the coupling of electrical excitations in superconducting qubits to mechanical oscillators [5,6], readout of quantum information has been demonstrated [7,8] and even the coupling of a spin to a mechanical resonator has been shown [9]. The necessary interaction has often been obtained by electric fields, e.g., in capacitive drum resonators, but also, in some cases, coupling of superconducting quantum circuits to surface acoustic waves has been demonstrated [10,11]. Another suitable mechanism for information transfer, however, can make use of the coupling of magnetic fields to spin-wave modes in a magnon resonator. Indeed, the coupling of a magnon mode in a

macroscopic yttrium iron garnet (YIG) sphere to a single qubit has already been demonstrated in 2015 [12] and an overview of hybrid quantum systems based on magnonics can be found in Ref. [13]. For downscaling and integration, however, smaller YIG structures are needed. Taking these results into account, it is a promising perspective to realize a alternative transfer mechanism by coupling magnons to mechanical oscillations in a nanomechanical resonator via magnetoelastic coupling. Obviously, YIG would be an ideal candidate for these resonators since it is the material with the lowest known Gilbert damping [14] and it exhibits extremely long lifetimes for spin waves (magnons) in the microsecond regime. As a single-crystalline garnet material with a Young's modulus of the same order of magnitude as that of silicon carbide, it is expected to also provide low losses for mechanical waves (phonons) [15] and may yield nanoresonators with high quality factors. An enhanced spin-lattice coupling observed in rare-earth-doped YIG or other rare-earth-based garnets might facilitate the magnon-phonon coupling; however, all alternative materials lack the long magnon lifetime necessary for

\*georg.schmidt@physik.uni-halle.de

possible applications (see, e.g., Ref. [16]). Furthermore, in macroscopic YIG spheres in the submillimeter range, the coupling of magnons to phonons has already been demonstrated [17]. Zhang *et al.* have shown that the coupling of magnons and phonons in YIG via magnetostrictive coupling is possible, but also that for a successful experiment a phonon frequency much bigger than the magnon line width is necessary.

Although YIG nanoresonators would thus advance this field, up to now no method has been known to shape three-dimensional (3D) nanostructures from monocrystalline YIG. Nanopatterning of thin films with reasonable quality has been demonstrated [18–22], but no patterning of nanosized freestanding resonators has been put forward.

Bridge- or cantilever-type YIG mechanical resonators with a size of 70  $\mu\text{m}$  or more have been demonstrated recently [23–25]. However, their size does not yet approach the dimensions necessary for integration and their resonance frequencies of approximately 70 kHz [23,24], or in one case 2.5 MHz [25], are far too low for the intended coupling. Furthermore, the bridges and cantilevers discussed are not magnon resonators and the experiments do not even address the magnonic quality. In two of the experiments [23,25], the spin dynamics were not investigated at all. In the third experiment [24], the spin dynamics were only detected indirectly by a damping of the 70 kHz mechanical oscillation at the ferromagnetic resonance (FMR) condition, but no information on the FMR line width or the magnon lifetime was provided.

Nevertheless, it would be extremely attractive if micron- or submicron-sized YIG bridges or cantilevers were available. The mechanical resonance frequencies in such structures may be easily engineered to fall in the range of typical magnon frequencies [26]. As a first step in this direction, we realize the fabrication of freely suspended YIG microbridges with very low damping for spin waves. Although the mechanical properties cannot yet be investigated in detail, the mechanical resonance frequencies calculated for their dimensions using the elastic properties of YIG fall into the range of several hundred megahertz and may even reach the gigahertz regime. In this frequency range, it may even be possible to achieve a direct coupling of magnons and phonons, whereas Zhang *et al.* [17] had to use a complicated parametric-pumping scheme with two different excitation frequencies.

## II. THREE-DIMENSIONAL NANOFABRICATION

Fabrication techniques for suspended-single-crystal nanostructures mostly use subtractive processing by removing material from a single crystal (bulk or layer). The most straightforward method uses focused-ion-beam (FIB) lithography to directly shape the desired structure from bulk or thin film [23–25,27]. Although it is very flexible in terms of possible geometries, this technique suffers from

possible damage to the crystal structure by extended beam tails, which might be detrimental to the magnetic properties of YIG. Also, it requires lateral access for the beam in order to remove the material underneath the suspended structure, preventing the creation of multiple structures in close vicinity to each other.

A good example for this problem is provided in Refs. [23–25], where—even at a distance of tens of micrometers from the structure—YIG had to be removed even for a cantilever of less than 1  $\mu\text{m}$  in width [23].

Alternatively, a crystalline film (resonator material) may be deposited on top of a sacrificial layer. The resonator itself is shaped by lithography and dry etching and only becomes freestanding when the underlying sacrificial layer is removed by highly selective wet chemical etching [28,29]. The resulting geometry, however, has several limitations. It is not truly three dimensional but is only a partly suspended two-dimensional (2D) structure. Also, the suspended resonator must be more narrow than the unsuspended pads to which it is attached. Otherwise, the pads are under-etched during the removal of the sacrificial layer. Unfortunately, no sacrificial layers are known for high-quality crystalline YIG films, which can only be deposited on garnet surfaces (especially gallium gadolinium garnet, GGG) and no selective wet etchants are available for these materials.

On the other hand, nanoscale additive fabrication of polycrystalline materials is achieved by electron-beam lithography, evaporation, and lift-off. A typical example is the fabrication of metallic air bridges, which has been well known for more than a decade [30–32]. The process allows for densely packed structures with high flexibility in terms of geometry. However, it requires low-temperature deposition of the material because of the limited thermal stability of electron-beam resists. This prevents its use for the patterning of monocrystalline materials such as YIG, which in most cases need to be deposited at elevated temperatures.

An alternative kind of deposition method for thin-film YIG has recently been demonstrated. Amorphous YIG films are deposited at room temperature on GGG using either pulsed-laser deposition (PLD) [33,34] or sputtering [35]. In a subsequent annealing step, the material adapts to the lattice structure of the substrate, resulting in thin single-crystalline YIG films. Surprisingly, the quality of these films in terms of damping surpasses the quality of thin films deposited at high temperature [33–35]. Because the deposition is done at room temperature, this deposition method is compatible with electron-beam lithography. In this way, the fabrication of laterally nanopatterned YIG with reasonably small Gilbert damping constants has been demonstrated recently [18,19,21]. Theoretically, this process also allows for the fabrication of beams and bridges when it is adapted to the patterning process used for metal bridges described above. Nevertheless, the higher kinetic energies of the deposited particles in PLD compared to

evaporation may necessitate a specially adapted resist profile to guarantee a successful lift-off. Further on, the recrystallization is more challenging. In a thin film, crystallization needs to progress only vertically from the substrate to the film surface (with a typical distance of 100 nm or less). In a bridge structure, however, the crystallization starts at the base of the supporting pillars, which are in contact with the substrate, and then needs to progress around bends across the entire span of the bridge in order to achieve a monocrystalline structure. Any additional nucleation site for crystallization may disturb the process and introduce an additional grain boundary. As we show in the following, it is possible to realize such a 3D lift-off process for YIG with the crystallization (which, indeed, starts at the substrate) extending throughout the complete bridge structure even over distances of several micrometers.

### III. PROCESSING

Figures 1(a)–1(d) schematically show the applied process flow. A thick PMMA layer on a  $\langle 111 \rangle$ -oriented GGG substrate is patterned using electron-beam lithography at different electron-acceleration voltages for the span (low voltage, LV) and pillars (high voltage, HV) of the bridges, respectively [Fig. 1(a)]. The pillars and the span of the bridge are exposed using PMMA as a resist and two different respective acceleration voltages. The span is exposed at 2.8 kV, while the acceleration voltage for the span is 4.5 kV. For both exposures, the area dose is  $100 \mu\text{C cm}^{-2}$ . The structures are developed for 60 s in isopropanol. The resulting structure after development of the e-beam resist is shown in Fig. 1(b). It exhibits holes down to the substrate for the pillars and a groove for the span of the bridge. At the sides, the groove has a slight undercut, which later facilitates the lift-off process. The amorphous YIG material is deposited onto the developed structure by PLD at room temperature [Fig. 1(c)]. The YIG is deposited

in 0.025 mbar of oxygen from a homemade target. The laser parameters are a wavelength of 248 nm, a fluence of  $2.5 \text{ J cm}^{-2}$ , and a repetition rate of 5 Hz. Annealing is performed in an oxygen atmosphere (99.997%) at ambient pressure and  $800^\circ\text{C}$  for 3 h. Subsequent lift-off and resist removal results in a bridge structure [Fig. 1(d)], which is finally annealed. Figure 2(a) shows a scanning-electron-microscopy (SEM) image of a YIG bridge (a) prior to and (b) after annealing. The bridge has a nominal span length of  $2 \mu\text{m}$  and a YIG layer thickness of approximately 110 nm. The length of the span does not change during the annealing step within the measurement accuracy of the SEM. For the experiment shown here, the pillars are not placed at the ends of the bridges. This design yields an overhang at the end to combine the investigation of short cantilevers fixed on one end only with that of bridge structures that are clamped at both ends. The resulting bridges and cantilevers are flat and strain free after the lift-off. Subsequent to annealing, the bridge itself remains mostly unchanged; however, the overhang is bent upward [Fig. 2(b)], indicating the presence of strain.

During the crystallization at more than  $800^\circ\text{C}$ , the lattice can reorder and a structure with very little or no strain is created. During cool-down, however, the difference between the thermal expansion coefficients of YIG and GGG can lead to a small deformation. The YIG now exhibits tensile strain. While in a continuous layer on a substrate this strain would lead to a change in lattice constant, the bridge can now follow the strain by deformation. By tilting the feet inward, the length of the span can be decreased, while tilting of the feet can also lead to the small upward bending of the overhang. The thermal-expansion coefficient for YIG is smaller than that of GGG by approximately  $2 \times 10^{-6} \text{ K}^{-1}$ . By cooling from  $800^\circ\text{C}$  to room temperature, the contraction of the YIG lattice is approximately 0.1% larger than for GGG. It should be noted that

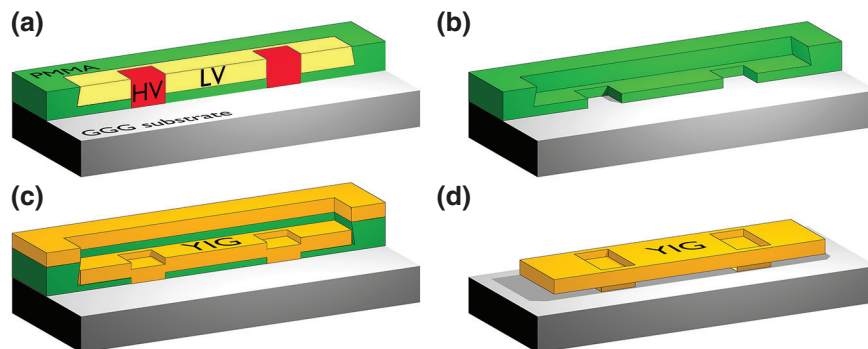


FIG. 1. A schematic drawing of the patterning process. (a) A resist (green) is exposed with two different acceleration voltages. A low-voltage exposure is used for the span of the bridge (yellow) and a high acceleration voltage (red) exposes the pillars down to the substrate. (b) After development, the void in the resist has the shape of the bridge and a slight undercut, which later facilitates the lift-off. (c) The YIG is deposited and the shape of the bridge becomes visible. It is important that the YIG on the resist surface is well separated from the bridge itself. (d) After lift-off, a freestanding bridge is obtained.



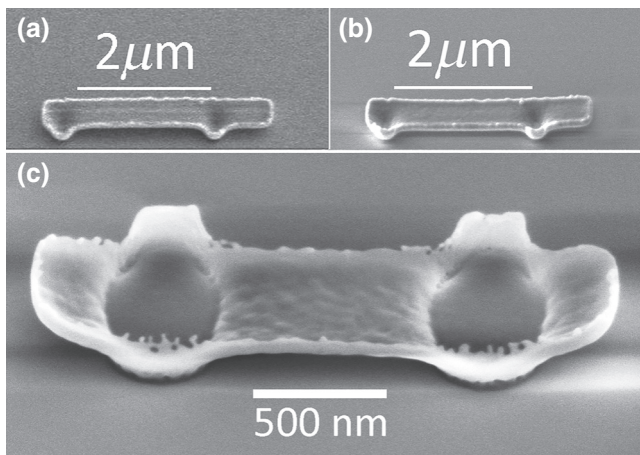


FIG. 2. SEM images of two different bridges. (a),(b) A larger bridge before and after annealing, respectively. (c) A smaller bridge after annealing. The deposited YIG has a nominal thickness of 110 nm.

any resulting shortening of the bridge is too small to be measured with the accuracy of our electron microscope.

Figure 2(c) shows a close-up view of an annealed YIG bridge with a span of 750 nm, also after annealing. The deposited YIG has a nominal thickness of 110 nm. The edges of this bridge are quite rough and show a lot of residue from the lift-off process. Obviously, these can be detrimental to the quality of mechanical resonances. As we show later, these residues can mostly be avoided or removed.

#### IV. STRUCTURAL CHARACTERIZATION

While the SEM images show that the molding of the material is successful, the local crystalline quality can only be assessed by transmission electron microscopy (TEM). Atomic-resolution TEM is performed on different bridges

after annealing. TEM samples from bridges are prepared using a focused gallium-ion-beam “FEI VERSA 3D” dual-beam microscope by the classic FIB *in situ* lift-out technique, as described, for instance, by Bals *et al.* [36]. Due to the electrically isolating substrate, this procedure is extended for the preparation of the sample after thermal treatment by depositing a thin conductive carbon layer via ion sputtering before transferring the sample to the FIB. As the first step in the preparation procedure inside the FIB, a 200-nm-thick carbon layer is deposited locally using the electron beam at 5 kV from the top through the bridge, to fill the space under the bridge with carbon. The hole under the bridge is filled by locally cracking the organometallic complex gas from the platinum gas-injection system of the FIB with a 5-kV electron beam. After lift-out, the TEM lamellae are mounted onto a grid, thinned down to a thickness below 150 nm, and stepwise cleaned on both sides from amorphous material by operating the ion beam of the FIB at 5 kV, 2 kV, and 1 kV. HRTEM images from these samples are obtained using a JEOL JEM-4010 TEM operated at 400 kV.

Figure 3(a) shows a cross-section view of a small bridge with a span of approximately 850 nm and a height between span and substrate of 75 nm. The sample is prepared using a focused ion beam and cut along a {011} plane perpendicular to the surface. The viewing direction of the TEM is along (011) with a small tilt angle.

The pillars, which are in direct contact with the substrate, show an epitaxial monocrystalline lattice, as also observed for large-area deposition by Hauser *et al.* [33]. The transition to the span where the material is thinner shows a number of defects that are likely due to the partially relieved shear strain that can be expected in this location.

The span of the bridge, however, appears to be monocrystalline and of perfect crystallinity except for a single defect in the center [Fig. 3(b)]. This defect is a

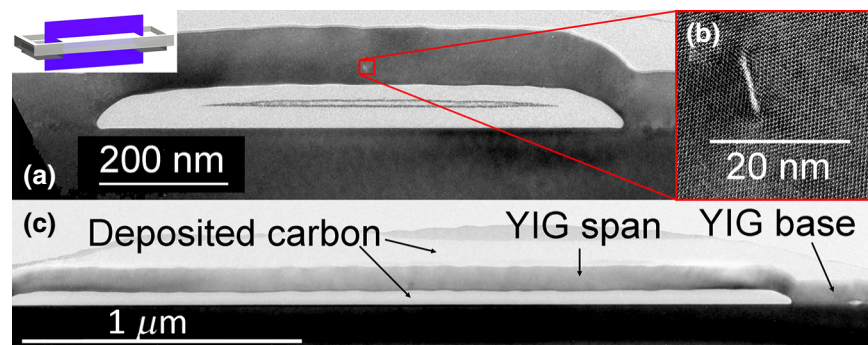


FIG. 3. TEM images for bridges with a nominal thickness of the span of 110 nm. (a) A bridge with a span of length approximately 850 nm and a height of 75 nm underneath the span. (b) Higher magnification shows single-crystalline material with a single defect in the center of the bridge. (c) A TEM cross section of a bridge with increased length. Even for a length of  $2.8 \mu\text{m}$ , the bridge is free of defects except for the central defect. Above and below the bridge, a carbon film is visible, which has been deposited using the electron beam during TEM preparation to protect the surface of the bridge. The insert in the top left corner shows the size and orientation of the TEM lamella prepared from the bridge.

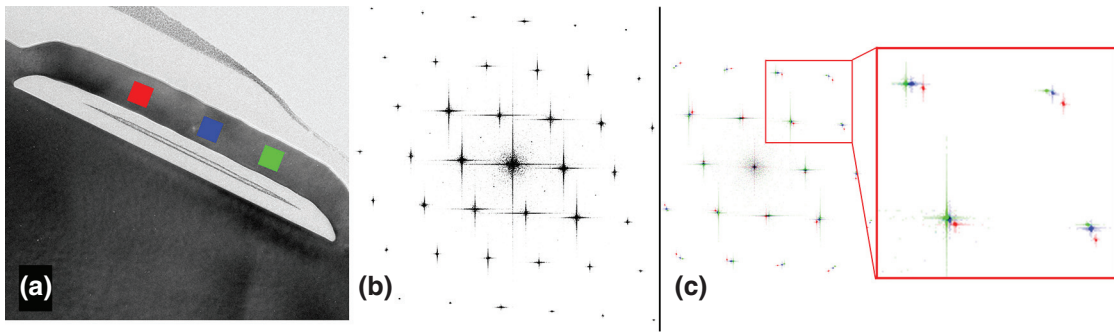


FIG. 4. FFTs of different parts of the lattice of a single bridge. (a) A TEM image of a bridge with three different square areas color coded in red, green, and blue. (b) A FFT of the substrate. (c) For the color-coded areas, the FFT of the lattice is superimposed using the same color code. An enlargement of the superposition (frame) shows that a very small rotation of the lattice has taken place, which is in the range of approximately  $1^\circ$ . All FFTs are obtained from images with the same orientation and magnification.

consequence of the crystallization process as described below. To investigate possible differences in the lattice orientation of the substrate and the bridge, FFTs of TEM images are taken at different spots of the sample. A comparison of FFTs from the substrate and the bridge shows that except for a minute lattice rotation, the lattice parameter and orientation are identical for the substrate and the bridge. This is expected due to the excellent lattice match between YIG and GGG (mismatch approximately 0.06%). In addition, FFTs from different points of the bridge are superimposed to see whether the lattice orientation varies along the bridge (Fig. 4). A color-coded overlay of the FFTs on the left, right, and center of the span shows that the crystal orientations on both sides are tilted with respect to each other, with a tilt angle of about  $1^\circ$ . A similarly small rotation is observed when comparing FFTs from the bridge and the substrate. From these results, we can deduce that crystallization starts simultaneously at both pillars, where the material is strained. Thus the two crystallization fronts may be slightly tilted with respect to each other. When they meet at the center of the span, the resulting mismatch can only be compensated for by the formation of a crystal defect such as the small-angle grain boundary observed at the center of the bridge. In addition, this mechanism explains the small rotation of the left- and right-hand parts of the bridge with respect to each other and with respect to the substrate.

To investigate the influence of the bridge size on the crystallinity, cross-section TEM images of longer bridges also are studied [Fig. 3(c)]. Even for a length of  $2.8 \mu\text{m}$ , a similar quality of the span (which is the functional part of the resonator) is obtained.

## V. SPIN DYNAMICS

Because of the reduced amount of material, it is not possible to measure the saturation magnetization  $M_S$  of the bridges directly using magnetometry methods. From previous experiments, we know that YIG layers fabricated by

room-temperature deposition and annealing under similar conditions exhibit  $M_S$  up to 27% below the bulk value of  $\mu_0 M_S \approx 180 \text{ mT}$  [37]. We would like to note that the  $M_S$  value used for the micromagnetic simulations (132 mT) is in excellent agreement with these results.

In order to obtain a detailed and accurate measurement of the local dynamic properties, we perform time-resolved scanning Kerr microscopy (TRMOKE) experiments on a 110-nm-thick YIG bridge. Using this method, it is possible to image directly the different resonant magnon modes in individual bridge structures. To achieve the necessary high-frequency excitation of the YIG structures, an impedance-matched coplanar waveguide (CPW) is deposited by electron-beam lithography and lift-off processes onto the sample. The CPW is positioned such that an array of bridges is located in the gap between the signal line and the ground plane [inset of Fig. 7(a)]. The investigated bridge has a width of 600 nm and a span length of  $3 \mu\text{m}$ . The thickness of the deposited YIG film is 110 nm and the gap under the span is 100 nm. The sample is deposited using the parameters described in section Processing. For the TRMOKE measurements, we use a frequency-doubled femtosecond laser operating at 520 nm to illuminate the sample in a scanning optical microscope, with polarization analysis. A detailed description of this method is presented in the work of Farle *et al.* [38]. In our TRMOKE measurements, the magnetization is excited by a continuous-wave microwave magnetic field that is phase synchronized to the optical-probe pulses, i.e., the sampling is stroboscopic. In order to allow for lock-in amplification of the magneto-optical signal, the rf excitation is modulated [39,40]. The spatial resolution of the measurements presented in this manuscript is diffraction limited to about 300 nm.

The spatially resolved measurements are performed with the external magnetic field oriented along the bridge, allowing for the excitation of the backward-volume modes (BVMs) with  $k$  vectors along the bridge and the Damon-Eshbach modes (DEMs) with  $k$  vectors at an angle

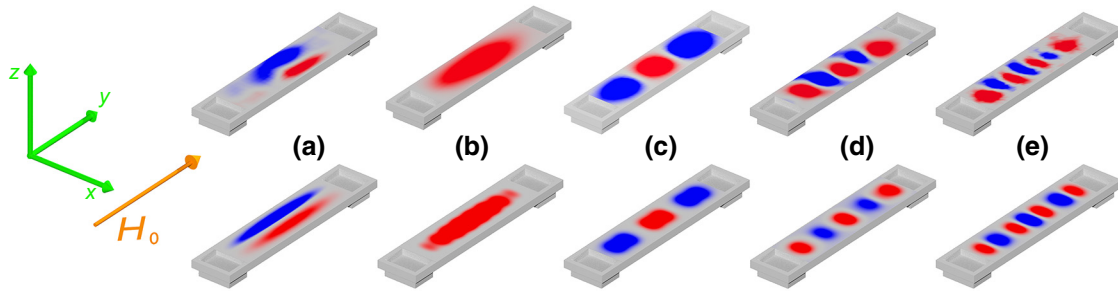


FIG. 5. TRMOKE images of standing spin-wave modes and simulations. The top row shows TRMOKE results for (b) the main mode, (a) one DEM, and (c)–(e) three different BVMs. The measurement parameters (given as magnetic field, excitation frequency) are as follows: (a) 11.96 mT, 2 GHz; (b) 21.95 mT, 2 GHz; (c) 25.61 mT, 2 GHz; (d) 89.72 mT, 4 GHz; (e) 92.52 mT, 4 GHz. The modes are imaged at the peak amplitude of the respective resonance. The bottom row shows the corresponding simulation results from simulations at fixed respective magnetic fields (as described below). The simulation parameters are as follows: (a) 19.4 mT, 2.32 GHz; (b) 19.4 mT, 2.00 GHz; (c) 19.4 mT, 1.85 GHz; (d) 83.8 mT, 3.73 GHz; (e) 83.8 mT, 3.66 GHz. The coordinate system on the left-hand side shows the orientation of the external magnetic field,  $H_0$ . The raw data of such measurements is available in the format as shown below in Figs. 9 and 10. In order to visualize the position on the respective bridge, the noise is reduced by averaging and the color scale is modified and normalized for better identification of the antinodes of the spin-wave excitation.

of  $90^\circ$ . Figure 5 (top row) shows a number of different modes for an increasing magnetic field. The fundamental mode with only one antinode is shown in Fig. 5(b). Three standing BVMs with nodes distributed along the bridge are shown in Figs. 5(c)–5(e), while a DEM mode shows a node extending along the bridge [Fig. 5(a)]. It is clearly visible that the magnons are localized in the span of the bridge and no direct coupling to the pillars or beyond is observed.

While the direct phase-resolved imaging of localized standing spin waves in permalloy nanodisks by TRMOKE has already been demonstrated [41], this kind of imaging has not been achieved in YIG 3D nanoresonators or in 2D YIG nanostructures. For larger 2D structures of several micrometers in size, the spin-wave intensity can be measured using micro-Brillouin light scattering [42]; however, this method does not provide any phase information, while TRMOKE allows us to map the standing magnon modes in detail and to show the main resonance modes of five different symmetries in a single structure, none of them edge modes.

We also model the different magnon modes using the MUMAX3 code [43]. Figure 5 (bottom row) shows the respective simulations, which are in good agreement with our experiments. The simulated bridge has a width of 600 nm and a span length of 2700 nm. The thickness of the deposited YIG film is 110 nm and the gap under the span is 100 nm. The pillars are  $300 \text{ nm} \times 600 \text{ nm} \times 110 \text{ nm}$ . The gyromagnetic ratio  $\gamma$  obtained in the simulations is  $178 \text{ GHz T}^{-1}$ , which is close to the value obtained from the MOKE data ( $171 \text{ GHz T}^{-1}$ , Fig. 6). The saturation magnetization is fitted to match the spin-wave patterns, resulting in a value of  $\mu_0 M_S \approx 132 \text{ mT}$ , which is in good agreement with that of large-area films deposited by the same method [33]. After relaxing the magnetization of the structure in the external magnetic field  $H_0$  in the

$x$  direction, a small field step perpendicular to the surface ( $z$ ) is applied. The following precession in the  $z$ - $y$  plane is recorded and a FFT is performed. In the FFT, the main oscillations are identified as peaks in the amplitude. The images are obtained by locally evaluating the amplitude and phase of the precession and transforming them into a color (intensity = amplitude; positive phase, red; negative phase, blue).

In order to obtain a better understanding in terms of the magnetization dynamics in the YIG nanobridges, FMR spectra are measured by TRMOKE on a single spot in the center of the bridge for several frequencies. Such

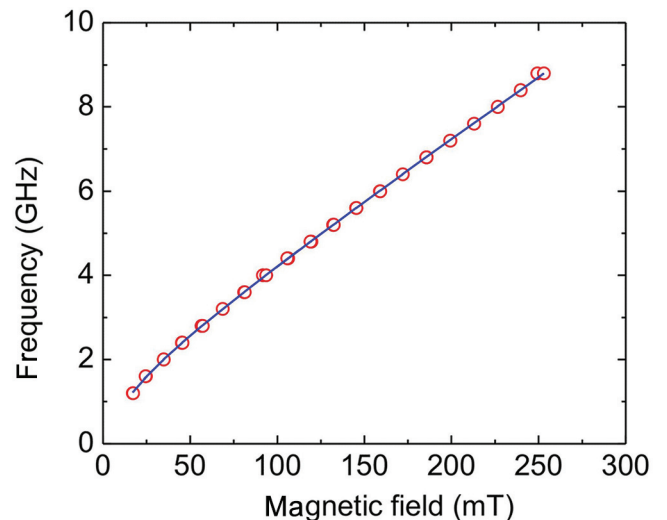


FIG. 6. The resonance frequency plotted as a function of the applied magnetic field. The results agree nicely except for small deviations at low magnetic fields. The red circles show the measured data, while the blue line is the respective fit using the Kittel formula.



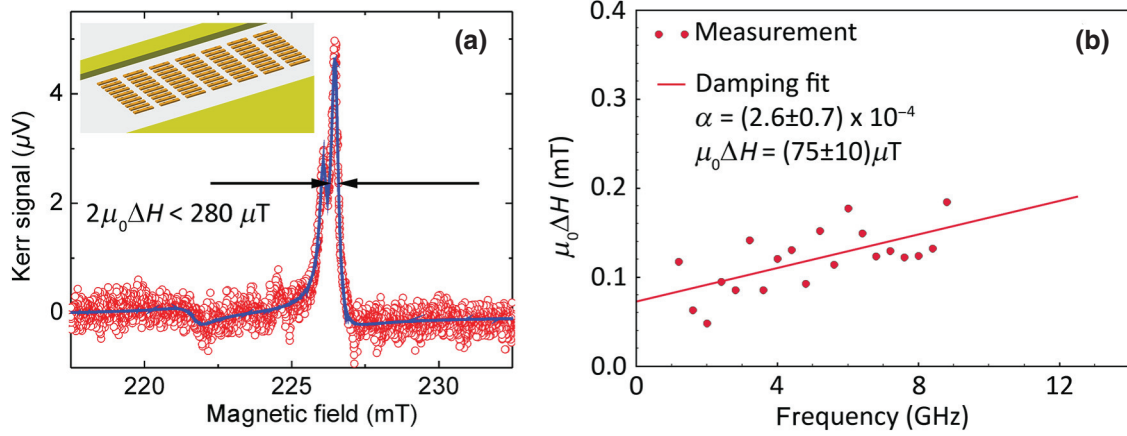


FIG. 7. (a) A FMR spectrum obtained by TRMOKE at the center of a single bridge, excited at 8 GHz. The red circles show the measured data, while the blue line is a fit using three Lorentzian line shapes. The arrows are a guide to the eye, showing an upper limit for the full width at half maximum, which is  $2\mu_0\Delta H$ . The half width at half maximum,  $\mu_0\Delta H$ , is mostly referred to in the literature as the line width. The measurement, which is performed on a single spot with a diameter of approximately 300 nm, shows two very sharp lines with a small overlap. The line width,  $\mu_0\Delta H$ , is smaller than  $140 \mu\text{T}$ . The insert shows a sketch of an array of bridges located between the signal line and ground of a CPW. (b) The line width plotted versus the frequency. A least-mean-square fit yields a slope corresponding to a Gilbert damping coefficient of  $(2.6 \pm 0.7)^{-4}$ .

a resonance spectrum is shown in Fig. 7(a), where the main resonance peak has a line width of approximately  $140 \mu\text{T}$  at 8 GHz. This value is among the smallest values reported for PLD-grown thin-film material so far. Only material grown by liquid-phase epitaxy exhibits smaller line widths. From our data, we find a Gilbert damping value of the main resonance of  $\alpha \approx (2.6 \pm 0.7) \times 10^{-4}$  [Fig. 7(b)]. This value is also among the lowest values reported for YIG grown by PLD at elevated temperatures. The inhomogeneous line width at zero field is  $\mu_0\Delta H_0 =$

$75 \pm 10 \mu\text{T}$ . For the given configuration, these numbers can also be translated into spin-wave lifetimes, resulting in 220 ns (3.2 GHz), 160 ns (5.2 GHz), and 120 ns (8.4 GHz).

It should be noted that in the context of recent publications [18–22], this result is completely unexpected. A reasonable magnon lifetime has only been demonstrated for extended waveguides [22] of width  $2.5 \mu\text{m}$  and length  $50 \mu\text{m}$ . In all other cases [18–21], the nanostructures have exhibited a damping (if provided) of  $\alpha \geq 8 \times 10^{-4}$  or a line width of  $400 \mu\text{T}$  at 9.8 GHz. Although these measurements were all done on a two-dimensionally patterned material, these values are much higher than those presented here for freestanding 3D structures. One reason for this low damping may be the extremely high quality of the YIG films fabricated by the deposition process described in Ref. [33]. While the origin of the low damping in these films is still under investigation, at least one hint can be found in the work of Sun *et al.* [44]. They see a dependence of damping on the surface roughness of YIG films deposited by PLD related to two-magnon scattering. Our findings show that material deposited as described in Ref. [33] exhibits an extremely low surface roughness. Furthermore, the span of the bridge in which the main resonance mode is localized is decoupled from the substrate. Finally, our method allows for the investigation of individual nanostructures rather than an ensemble, avoiding the influence of small variations between individual structures, as discussed below.

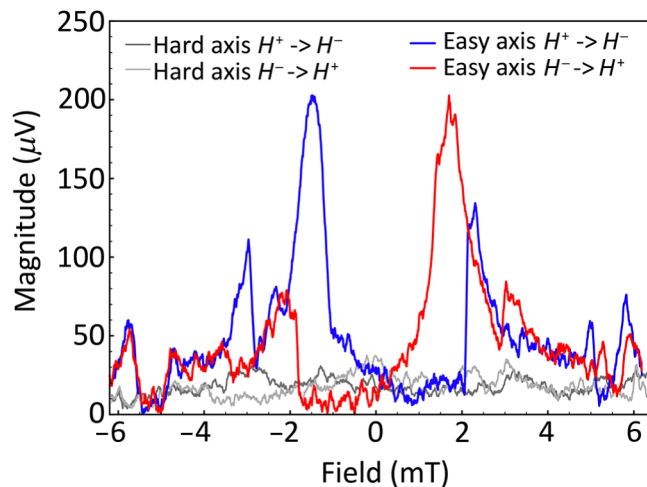


FIG. 8. TRMOKE measurement of the static switching behavior. While sweeping the field through the static hysteresis, the magnitude of the rf susceptibility is determined as a function of the applied magnetic field. The hysteretic part of the measurement represents the hysteresis of the static switching of the magnetization.

To determine the effective saturation magnetization  $M_{\text{eff}}$ , which also contains any anisotropy, and the gyromagnetic ratio  $\gamma$ , the resonance fields of the main FMR line are measured as a function of the frequency (Fig. 6) and the

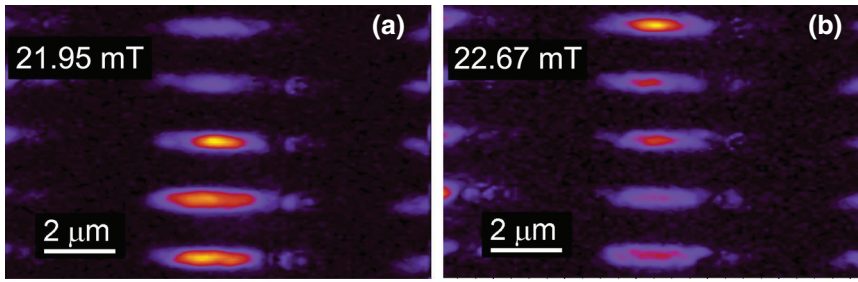


FIG. 9. Two TRMOKE images obtained at a frequency of 2 GHz, showing five adjacent bridges at two different magnetic fields, respectively. In both images, at least one of the bridges shows an intense resonance of the mode with only one antinode. Apparently, the resonance field between bridges can vary at least by 0.8 mT.

data are fitted using the Kittel formula:

$$\omega = \mu_0 \gamma \sqrt{H_{\text{FMR}}(H_{\text{FMR}} + M_{\text{eff}})}. \quad (1)$$

The fit yields  $\gamma = (180.3 \pm 0.6) \text{ GHz T}^{-1}$  and  $\mu_0 M_{\text{eff}} = (0.125 \pm 0.003) \text{ T}$ .

In addition to the dynamic properties, TRMOKE also allows us to investigate the static switching behavior of individual nanobridges. For this, we use the method in an off-resonant fashion around zero field (Fig. 8). Here, the phase and the magnitude of the rf susceptibility are used to detect the switching, as first demonstrated in Ref. [45]. For the measurement, the microwave frequency is set to 1 GHz. The probing light spot is placed at the center of the same bridge. The magnitude of the response depends on the internal magnetic field and is therefore sensitive to the relative alignment of magnetization and applied magnetic field. Hysteretic behavior is found when the magnetization and the applied magnetic field are antiparallel. From this, we determine a coercive field of  $\mu_0 H_C \approx 2 \text{ mT}$  for the bridge (lateral dimensions of the span:  $600 \text{ nm} \times 3 \mu\text{m}$ ) when the magnetic field is aligned with the long axis of the bridge structure (the easy axis). For a magnetic field aligned along the short axis of the bridge (the hard axis), we find no hysteretic behavior, as expected. This coercive field is considerably larger than for comparable continuous YIG films of the same thickness, where we find coercive fields of less than 0.1 mT [33]. The enhanced coercive fields in the YIG nanobridges are expected and are a consequence of the shape anisotropy and the increased contribution of the domain-wall nucleation energy to the magnetization reversal in nanostructures.

In the FMR spectrum, a second line is also visible, which partly overlaps with the main peak. Spatially resolved measurements indicate that the two halves of the span, which are separated by the central crystalline defect, differ in resonance field by approximately  $100 \mu\text{T}$  at 8 GHz. This can be explained by the rotation of the two sides observed in TEM. When the field is applied exactly along one half of the bridge, the small tilt of the other half can shift the resonance field in the order of  $100 \mu\text{T}$  at 8 GHz simply because a very small demagnetizing field is added to the external field. For one degree of tilt, this modification can be as large as 0.05% of the resonance field, which is sufficient to explain the observed resonance-line shift.

In addition, the spatial resolution of TRMOKE also allows us to investigate the variation of the resonance field between different bridges and between different parts of a single bridge (namely the span and overhang),

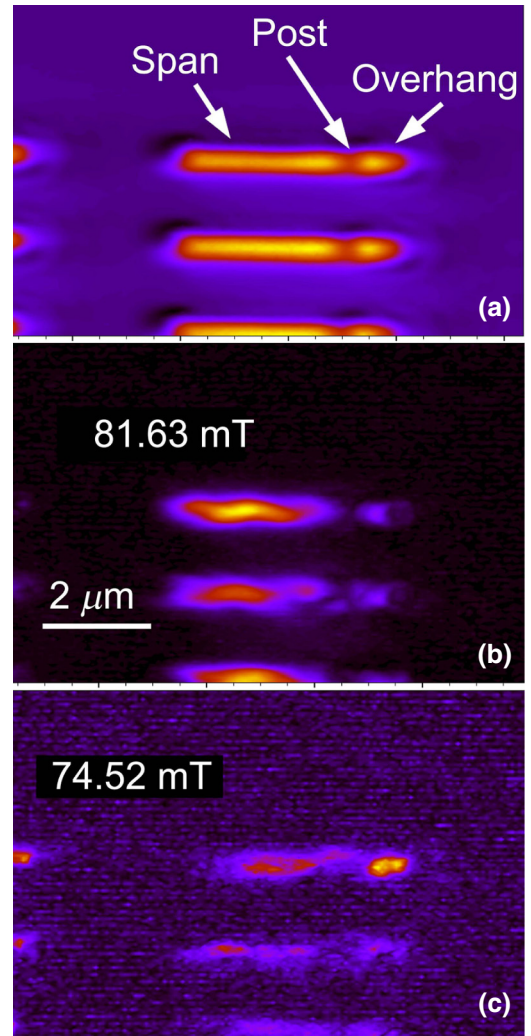


FIG. 10. (a) An optical topography image of several bridges. (b),(c) Two TRMOKE images of the same area, acquired at a frequency of 6 GHz at different respective magnetic fields. In the topography image, we can clearly discern the span of the bridge, the base, which is slightly darker, and the overhang at the end. The main resonance of the span with one antinode is shown in (b), while in (c) a similar mode for the overhang of the same bridge is observed. The resonance fields differ by 7 mT.



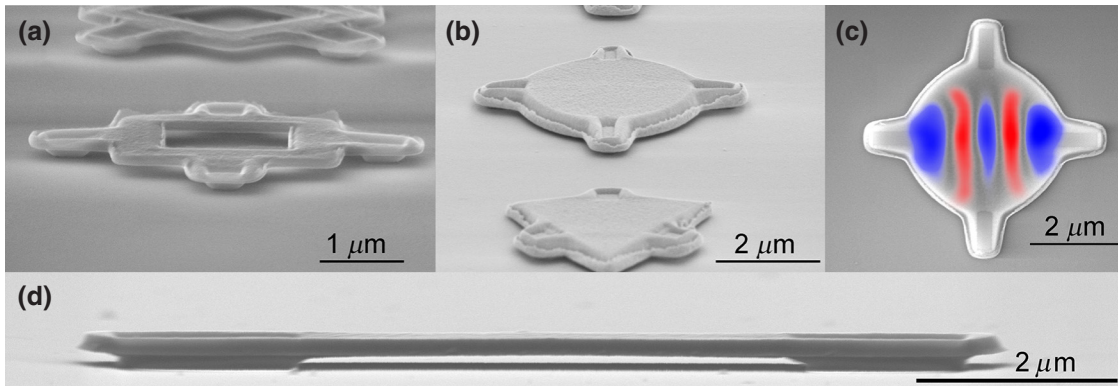


FIG. 11. SEM images of more complex resonators. The process allows us to fabricate various shapes such as (a) open squares or (b) disks and triangles. (c) A TRMOKE image of a standing BVM measured on a disk resonator overlaid on an SEM image of the same structure. For these structures, the nominal YIG thickness is 210 nm. (d) A bridge on which a postannealing wet-etch is applied. The artifacts at the seam of the structure are strongly reduced.

respectively. Figure 9 shows TRMOKE images of five different bridges obtained simultaneously and repeated for two different magnetic fields but at the same excitation frequency. For individual bridges, the main resonance (only one antinode) appears at fields that vary by almost 0.8 mT, respectively.

The resonance in the overhang of a bridge can only be imaged by sweeping the field over a wider range. Figure 10 shows that the overhang also exhibits a localized resonance. The resonance field is, however, offset by approximately 7 mT from the main resonance field of the corresponding span. This shift can be caused by the different strains in the span, which is pinned on both sides, and the overhang, which is pinned only on one side, as well as by the different sizes of the two regions. As the resonance does not extend into the foot of the bridge, the  $k$  vector is determined by the length of the area on resonance, as we no longer observe a true uniform mode but a standing spin wave with zero nodes.

It should be noted that the fabrication process is not limited to simple bridge geometries but is highly flexible and can be extended to more complex structures, as shown in the examples of Fig. 11, paving the way for a number of applications and experiments. Again, the magnetic excitations are also well defined and can be directly imaged. The SEM image and MOKE data in Fig. 11(c) are obtained from the very same structure. We also try to reduce the edge and surface roughness, which may cause the mechanical resonance properties to deteriorate, by using an optimized multilayer resist and a postannealing wet-etch step. As a result, an improved bridge with smoother edges is shown in Fig. 11(d).

## VI. DISCUSSION

It is possible to fabricate 3D YIG nanobridges using electron-beam lithography, room-temperature PLD, and lift-off. The structural characterization shows that

crystallization during the annealing process progresses throughout the bridge on a length scale of more than one micrometer, leading to an undisturbed lattice with only very few defects. The span of the bridge typically contains a single crystal defect. Previously, a similar crystallization process has only been presented in thin films rather than in a complex 3D nanostructures over a range of several micrometers. The damping does not reach the record values of low-temperature-grown YIG layers but is still in the range of high-quality PLD-grown YIG films. The minimum line width of 140  $\mu$ T at 8 GHz for a single bridge is well in the range of high-quality thin-film material and various resonant magnon modes can be identified in TRMOKE. Both the line width and the damping thus rival those obtained for large-area thin films deposited at higher temperatures. The mechanical resonances of the YIG bridges have yet to be characterized; nevertheless, an estimate of the possible resonance frequencies can be given. According to Yang *et al.* [46], the resonance frequency of a so-called doubly clamped beam, which corresponds to the span of our bridge, is approximately

$$f_{\text{res}} \approx 1.03 \frac{t}{L^2} \sqrt{\frac{E}{\rho}}, \quad (2)$$

where  $E$  is the Young's modulus of YIG ( $2 \times 10^{11}$  Pa) [47],  $\rho$  is the density ( $5.17 \text{ g cm}^{-3}$ ) [47],  $t$  is the thickness, and  $L$  is the length of the beam. Using these parameters with a thickness of 150 nm and a length of 1  $\mu$ m, a resonance frequency of 964 MHz is expected, while the same beam with a length of 500 nm resonates at 3.86 GHz, which is well in the range of typical magnons as measured in our experiments.

Obviously, the detection technique used in Refs. [23–25] is not applicable here. While in these experiments the mechanical resonance frequencies were only a few megahertz or even below 100 kHz, our resonators require

detection at frequencies of almost 1 GHz or more where piezoexcitation is no longer possible. Also, the size of our structures does not allow for the interferometric detection of the vibrational modes. It should be noted that in Refs. [24] and [25], the width of the structures was more than 5  $\mu\text{m}$ . In Ref. [23], the structure was more narrow and to allow for optical access for the interferometer, it was even necessary to integrate a large-area mirror at the end of the cantilever. Access to mechanical resonances in small bridges may be obtained by an alternative method, as demonstrated in Ref. [26]. However, this complex experiment is beyond the scope of the present work but will be addressed elsewhere.

For further development of the method, the next steps will be to fabricate more complex resonators that can not only host magnons with high quality factors but are also suitable for the characterization of mechanical vibrational modes. In addition, statistics need to be obtained by TRMOKE on the variation and reproducibility of resonance frequencies in nominally identical resonators, which are crucial for applications where the exact behavior needs to be predictable.

Possible applications for the nanoresonators can be found in various areas. Spin cavitronics, for example, investigates strong coupling of cavity resonator modes to magnon modes in macroscopic magnetic samples (typically YIG). In these experiments, the current technology uses large-volume YIG samples coupled to macroscopic planar superconducting microwave resonators [48] or large cavities [49]. Our YIG nanoresonators might be deposited over micron-sized superconducting coplanar waveguides, allowing for more complex experiments. In spin caloritronics, YIG bridges may be used to create large and extremely well-defined temperature gradients, because the span of the bridge is thermally decoupled from the substrate. It should be noted that a temperature difference of only 1 K over a bridge with a length of 1  $\mu\text{m}$  corresponds to a temperature gradient of  $10^6 \text{ K m}^{-1}$ . If coupling between phonons and magnons in the nanoresonators can be established, even an application for readout of qubits or conversion of quantum information between the microwave and the optical regime may be possible. Therefore the technology platform presented here may pave the way for downscaling, allowing these schemes to be realized on the micron scale or below and facilitating future integration of qubits.

### ACKNOWLEDGMENTS

This work was supported by the German Research Foundation (DFG) via the collaborative research centers SFB 762 (TP B9) and TRR 227 (TP B02). We thank the Max-Planck-Institut für Mikrostrukturphysik for making the JEOL JEM-4010 TEM available for our experiments.

- [1] A. P. Reed, K. H. Mayer, J. D. Teufel, L. D. Burkhardt, W. Pfaff, M. Reagor, L. Sletten, X. Ma, R. J. Schoelkopf, E. Knill, and K. W. Lehnert, Faithful conversion of propagating quantum information to mechanical motion, *Nat. Phys.* **13**, 1163 (2017).
- [2] R. W. Andrews, A. P. Reed, K. Cicak, J. D. Teufel, and K. W. Lehnert, Quantum-enabled temporal and spectral mode conversion of microwave signals, *Nat. Commun.* **6**, 10021 (2015).
- [3] F. Lecocq, J. B. Clark, R. W. Simmonds, J. Aumentado, and J. D. Teufel, Mechanically Mediated Microwave Frequency Conversion in the Quantum Regime, *Phys. Rev. Lett.* **116**, 043601 (2016).
- [4] C. F. Ockeloen-Korppi, E. Damskägg, J.-M. Pirkkalainen, T. T. Heikkilä, F. Massel, and M. A. Sillanpää, Low-Noise Amplification and Frequency Conversion with a Multiport Microwave Optomechanical Device, *Phys. Rev. X* **6**, 041024 (2016).
- [5] A. D. O'Connell, M. Hofheinz, M. Ansmann, R. C. Bialczak, M. Lenander, E. Lucero, M. Neeley, D. Sank, H. Wang, M. Weides, J. Wenner, J. M. Martinis, and A. N. Cleland, Quantum ground state and single-phonon control of a mechanical resonator, *Nature* **464**, 697 (2010).
- [6] J. M. Pirkkalainen, S. U. Cho, J. Li, G. S. Paraoanu, P. J. Hakonen, and M. A. Sillanpää, Hybrid circuit cavity quantum electrodynamics with a micromechanical resonator, *Nature (London)* **494**, 211 (2013).
- [7] M. D. LaHaye, J. Suh, P. M. Echternach, K. C. Schwab, and M. L. Roukes, Nanomechanical measurements of a superconducting qubit, *Nature* **459**, 960 (2009).
- [8] Y. Chu, P. Kharel, W. H. Renninger, L. D. Burkhardt, L. Frunzio, P. T. Rakich, and R. J. Schoelkopf, Quantum acoustics with superconducting qubits, *Science* **358**, 199 (2017).
- [9] S. G. Carter, A. S. Bracker, G. W. Bryant, M. Kim, C. S. Kim, M. K. Zalalutdinov, M. K. Yakes, C. Czarnocki, J. Casara, M. Scheibner, and D. Gammon, Spin-Mechanical Coupling of an InAs Quantum Dot Embedded in a Mechanical Resonator, *Phys. Rev. Lett.* **121**, 246801 (2018).
- [10] P. Arrangoiz-Arriola, E. A. Wollack, M. Pechal, J. D. Witmer, J. T. Hill, and A. H. Safavi-Naeini, Coupling a Superconducting Quantum Circuit to a Phononic Crystal Defect Cavity, *Phys. Rev. X* **8**, 031007 (2018).
- [11] A. Bienfait, K. J. Satzinger, Y. P. Zhong, H. S. Chang, M. H. Chou, C. R. Conner, É. Dumur, J. Grebel, G. A. Peairs, R. G. Povey, and A. N. Cleland, Phonon-mediated quantum state transfer and remote qubit entanglement, *Science* **364**, 368 (2019).
- [12] Y. Tabuchi, S. Ishino, A. Noguchi, T. Ishikawa, R. Yamazaki, K. Usami, and Y. Nakamura, Coherent coupling between a ferromagnetic magnon and a superconducting qubit, *Science* **349**, 405 (2015).
- [13] D. Lachance-Quirion, Y. Tabuchi, A. Gloppe, K. Usami, and Y. Nakamura, Hybrid quantum systems based on magnonics, *Appl. Phys Express* **12**, 070101 (2019).
- [14] T. Kasuya and R. C. LeCraw, Relaxation Mechanisms in Ferromagnetic Resonance, *Phys. Rev. Lett.* **6**, 223 (1961).
- [15] R. C. LeCraw, E. G. Spencer, and E. I. Gordon, Extremely Low Loss Acoustic Resonance in Single-Crystal Garnet Spheres, *Phys. Rev. Lett.* **6**, 620 (1961).

- [16] J. F. Dillon, Ferrimagnetic resonance in rare-earth-doped yttrium iron garnet. III. Linewidth, *Phys. Rev.* **127**, 1495 (1962).
- [17] X. Zhang, C.-L. Zou, L. Jiang, and H. X. Tang, Cavity magnomechanics, *Sci. Adv.* **2**, e1501286 (2016).
- [18] M. B. Jungfleisch, W. Zhang, W. Jiang, H. Chang, J. Sklenar, S. M. Wu, J. E. Pearson, A. Bhattacharya, J. B. Ketterson, M. Wu, and A. Hoffmann, Spin waves in micro-structured yttrium iron garnet nanometer-thick films, *J. Appl. Phys.* **117**, 17D128 (2015).
- [19] S. Li, W. Zhang, J. Ding, J. E. Pearson, V. Novosad, and A. Hoffmann, Epitaxial patterning of nanometer-thick  $Y_3Fe_5O_{12}$  films with low magnetic damping, *Nanoscale* **8**, 388 (2015).
- [20] M. Collet, X. de Milly, O. D'Allivy Kelly, V. V. Naletov, R. Bernard, P. Bortolotti, J. Ben Youssef, V. E. Demidov, S. O. Demokritov, J. L. Prieto, M. Muñoz, V. Cros, A. Anane, G. de Loubens, and O. Klein, Generation of coherent spin-wave modes in yttrium iron garnet microdiscs by spin-orbit torque, *Nat. Commun.* **7**, 10377 (2016).
- [21] N. Zhu, H. Chang, A. Franson, T. Liu, X. Zhang, E. Johnston-Halperin, M. Wu, and H. X. Tang, Patterned growth of crystalline  $Y_3Fe_5O_{12}$  nanostructures with engineered magnetic shape anisotropy, *Appl. Phys. Lett.* **110**, 252401 (2017).
- [22] M. Collet, O. Gladii, M. Evelt, V. Bessonov, L. Soumah, P. Bortolotti, S. O. Demokritov, Y. Henry, V. Cros, M. Bailleul, V. E. Demidov, and A. Anane, Spin-wave propagation in ultra-thin YIG based waveguides, *Appl. Phys. Lett.* **110**, 092408 (2017).
- [23] Y.-J. Seo, K. Harii, R. Takahashi, H. Chudo, K. Oyanagi, Z. Qiu, T. Ono, Y. Shiomi, and E. Saitoh, Fabrication and magnetic control of  $Y_3Fe_5O_{12}$  cantilevers, *Appl. Phys. Lett.* **110**, 132409 (2017).
- [24] Y. Oikawa, H. Arisawa, S. Daimon, and E. Saitoh, Enhanced mechanical damping induced by non-linear magnetization dynamics, *Appl. Phys. Lett.* **113**, 142407 (2018).
- [25] H. Arisawa, S. Daimon, Y. Oikawa, Y.-J. Seo, K. Harii, K. Oyanagi, and E. Saitoh, Magnetomechanical sensing based on delta-E effect in  $Y_3Fe_5O_{12}$  micro bridge, *Appl. Phys. Lett.* **114**, 122402 (2019).
- [26] X. M. Henry Huang, C. A. Zorman, M. Mehregany, and M. L. Roukes, Nanoelectromechanical systems: Nanodevice motion at microwave frequencies, *Nature* **421**, 496 (2003).
- [27] T. M. Babinec, J. T. Choy, K. J. M. Smith, M. Khan, and M. Lončar, Design and focused ion beam fabrication of single crystal diamond nanobeam cavities, *J. Vac. Sci. Technol. B: Microelectron. Nanometer Struct.* **29**, 010601 (2011).
- [28] M. P. Schwarz, D. Grundler, I. Meinel, C. Heyn, and D. Heitmann, Micromechanical cantilever magnetometer with an integrated two-dimensional electron system, *Appl. Phys. Lett.* **76**, 3564 (2000).
- [29] D. W. Carr and H. G. Craighead, Fabrication of nanoelectromechanical systems in single crystal silicon using silicon on insulator substrates and electron beam lithography, *J. Vac. Sci. Technol. B: Microelectron. Nanometer Struct.* **15**, 2760 (1997).
- [30] A. Yacoby, M. Heiblum, D. Mahalu, and H. Shtrikman, Coherence and Phase Sensitive Measurements in a Quantum Dot, *Phys. Rev. Lett.* **74**, 4047 (1995).
- [31] M. E. Sherwin, J. A. Simmons, T. E. Eiles, N. E. Harff, and J. F. Klem, Parallel quantum point contacts fabricated with independently biased gates and a submicrometer airbridge post, *Appl. Phys. Lett.* **65**, 2326 (1994).
- [32] T. Borzenko, C. Gould, G. Schmidt, and L. Molenkamp, Metallic air-bridges fabricated by multiple acceleration voltage electron beam lithography, *Microelectron. Eng.* **75**, 210 (2004).
- [33] C. Hauser, T. Richter, N. Homonnay, C. Eisenschmidt, M. Qaid, H. Deniz, D. Hesse, M. Sawicki, S. G. Ebbinghaus, and G. Schmidt, Yttrium iron garnet thin films with very low damping obtained by recrystallization of amorphous material, *Sci. Rep.* **6**, 20827 (2016).
- [34] C. Hauser, C. Eisenschmidt, T. Richter, A. Müller, H. Deniz, and G. Schmidt, Annealing of amorphous yttrium iron garnet thin films in argon atmosphere, *J. Appl. Phys.* **122**, 083908 (2017).
- [35] H. Chang, P. Li, W. Zhang, T. Liu, A. Hoffmann, L. Deng, and M. Wu, Nanometer-thick yttrium iron garnet films with extremely low damping, *IEEE Magn. Lett.* **5**, 6700104 (2014).
- [36] S. Bals, W. Tirry, R. Geurts, Z. Yang, and D. Schryvers, High-quality sample preparation by low kV FIB thinning for analytical TEM measurements, *Microsc. Microanal.* **13**, 80 (2007).
- [37] P. Hansen, P. Röschmann, and W. Tolksdorf, Saturation magnetization of gallium-substituted yttrium iron garnet, *J. Appl. Phys.* **45**, 2728 (1974).
- [38] M. Farle, T. Silva, and G. Woltersdorf, in *Magnetic Nanostructures: Spin Dynamics and Spin Transport* (Springer-Verlag, Berlin, 2013), p. 37.
- [39] G. Woltersdorf, O. Mosendz, B. Heinrich, and C. H. Back, Magnetization Dynamics due to Pure Spin Currents in Magnetic Double Layers, *Phys. Rev. Lett.* **99**, 246603 (2007).
- [40] J. Stigloher, M. Decker, H. S. Körner, K. Tanabe, T. Moriyama, T. Taniguchi, H. Hata, M. Madami, G. Gubbiotti, K. Kobayashi, T. Ono, and C. H. Back, Snell's Law for Spin Waves, *Phys. Rev. Lett.* **117**, 037204 (2016).
- [41] F. Hoffmann, G. Woltersdorf, K. Perzlmaier, A. N. Slavin, V. S. Tiberkevich, A. Bischof, D. Weiss, and C. H. Back, Mode degeneracy due to vortex core removal in magnetic disks, *Phys. Rev. B* **76**, 014416 (2007).
- [42] V. E. Demidov, M. Evelt, V. Bessonov, S. O. Demokritov, J. L. Prieto, M. Muñoz, J. Ben Youssef, V. V. Naletov, G. de Loubens, and O. Klein, Direct observation of dynamic modes excited in a magnetic insulator by pure spin current, *Sci. Rep.* **6**, 32781 (2016).
- [43] A. Vansteenkiste, J. Leliaert, M. Dvornik, M. Helsen, F. Garcia-Sanchez, and B. Van Waeyenberge, The design and verification of MUMAX3, *AIP Adv.* **4**, 107133 (2014).
- [44] Y. Sun, Y.-Y. Song, H. Chang, M. Kabatek, M. Jantz, W. Schneider, M. Wu, H. Schultheiss, and A. Hoffmann, Growth and ferromagnetic resonance properties of nanometer-thick yttrium iron garnet films, *Appl. Phys. Lett.* **101**, 152405 (2012).
- [45] G. Woltersdorf and C. H. Back, Microwave Assisted Switching of Single Domain  $Ni_{80}Fe_{20}$  Elements, *Phys. Rev. Lett.* **99**, 227207 (2007).
- [46] Y. T. Yang, K. L. Ekinci, X. M. H. Huang, L. M. Schiavone, M. L. Roukes, C. A. Zorman, and M. Mehregany,



- Monocrystalline silicon carbide nanoelectromechanical systems, *Appl. Phys. Lett.* **78**, 162 (2001).
- [47] A. E. Clark and R. E. Strakna, Elastic constants of single-crystal YIG, *J. Appl. Phys.* **32**, 1172 (1961).
- [48] H. Huebl, C. W. Zollitsch, J. Lotze, F. Hocke, M. Greifenstein, A. Marx, R. Gross, and S. T. B. Goennenwein, High Cooperativity in Coupled Microwave Resonator Ferromagnetic Insulator Hybrids, *Phys. Rev. Lett.* **111**, 127003 (2013).
- [49] Y. Tabuchi, S. Ishino, T. Ishikawa, R. Yamazaki, K. Usami, and Y. Nakamura, Hybridizing Ferromagnetic Magnons and Microwave Photons in the Quantum Limit, *Phys. Rev. Lett.* **113**, 083603 (2014).